Inorganic Stimuli-Responsive Nanomembranes for Small-Scale Actuators and Robots

Ziao Tian, Yang Wang, Yimeng Chen, Borui Xu, Zengfeng Di, and Yongfeng Mei*

The term small-scale robotics describes a wide variety of miniature robotic systems, ranging from millimeter-sized devices down to autonomous mobile systems with dimensions measured in nanometers. These systems can perform complex tasks that are impossible for humans to accomplish or at scales that humans cannot reach. In recent years, the rapid advancement of small-scale robotics has benefited from the progress in synthesis and nanotechnology, providing access to nanomembranes with stimuli-responsive materials, such as phase transition materials, shape memory alloys, and palladium. These materials are 2D sheets with a thickness ranging from 5 to 500 nm, and they have the ability to change their shape reversibly under extremal stimuli. Together with strain engineering for deterministic assembly, various stimuli-responsive actuators and robots have been fabricated for medicine, manufacturing, and exploration by endowing them with the combined features of a continuously deformable structure, remote operation, and several degrees of freedom. Herein, the recent achievements in small-scale actuators and robots based on inorganic stimuli-responsive nanomembranes are reviewed and their advantages and properties highlighted.

1. Introduction

Small-scale robotics are smaller than conventional robotic systems, ranging from several millimeters to nanometers in size.[1] They can perform more complex tasks that are impossible for humans or at scales that humans cannot reach. Such robots possess a wide range of applications, including areas such as medicine,[2] manufacturing,[3] and exploration.[4] While

Prof. Z. Tian, Dr. Y. Wang, Dr. Y. Chen, Dr. B. Xu, Prof. Y. Mei
Department of Materials Science
State Key Laboratory of ASIC and Systems
Fudan University
220 Handan Road, Shanghai 200433, China
E-mail: yfm@fudan.edu.cn, meiyongfeng@hotmail.com

Prof. Z. Tian, Prof. Z. Di
State Key Laboratory of Functional Materials for Informatics
Shanghai Institute of Microsystem and Information Technology
Chinese Academy of Sciences
Shanghai 200050, China

large-scale robots have greatly progressed in terms of complexity, accuracy of motion control, and level of intelligence, robots at small scales must overcome many challenges related to their fabrication, control, and power delivery. Recently, because of the exciting advances in materials science including the development of stimuli-responsive materials and actuation schemes, the field of small-scale robotics is growing rapidly.[5–8] Stimuli-responsive materials have the ability to respond to external stimuli, such as light,[9] heat,[10] pH,[11] metal ions,[12] electric fields,[13,14] and magnetic fields.[15] By virtue of the fabrication techniques including traditional composite syntheses and printing, these stimuli-responsive materials have been utilized to construct diverse reconfigurable structures, from the nanoscale to the macroscale, that can reversibly switch their shape in response to different stimuli. Based on stimuli-responsive materials, various robots driven by actuators, which can convert a variety of energy types to kinetic energy, have been widely reported recently.[16–22] Compared with motor-driven robots, the actuator-driven robots exhibit a continuously deformable structure with several of degrees of freedom, which bridges the gap between machines and people.[18,19] Recent advances in actuator-driven robots have mainly focused on functional polymers with a relatively low stiffness, which restricts the loading capacity of the fabricated structures.[23] In addition, the responses of these functional polymers to external stimuli depend on the diffusion process of certain physical or chemical signals, limiting the actuation speed of the reconfigurable structures.[24] To avoid these drawbacks, researchers have resorted to stimuli-responsive inorganic materials (i.e., phase changing and shape memory alloys [SMAs], as well as palladium [Pd]) because these materials have a high power density and can offer fast responses. Traditional solid-bulk inorganics are typically and intrinsically rigid and brittle, properties which limit deformability associated with bending, stretching, and loading.[25] When the minimum lateral dimension is thinned at least two orders of magnitude, materials can convert from hard into soft and be shaped more easily.[26] This planar, flexible, stretchable, and easily deformable stimuli-responsive material is referred to as a stimuli-responsive nanomembrane (SNM). Because of their good elasticity, light weight, high deformability, and high transparency, SNMs can exhibit greater shape-changing capabilities and provide a stronger impetus for the development of soft robots, artificial

muscles, biomimetic devices, and beyond.[21,24,26] **Figure 1** pictorially shows the spectrum of small-scale robot approaches: from millimeter-scale robots built with polymer to nanometer robots built with SNMs. A swelling-induced microgel jumps at millimeter-scale dimensions is fabricated using microstereo-lithography techniques.[27] The smallest example of a micro-walker comprising anisotropic gold (Au) nanorod is fabricated and is at a scale smaller than that of human red blood cells. In this review, we mainly focus on the recent achievements in small-scale actuators and robots based on inorganic SNMs and highlight their advantages and properties.

## 2. Inorganic Stimuli-Responsive Materials Turn Soft

In 1991, Pierre De Gennes defined a soft material as one that can be easily deformed by external stresses, electric or magnetic fields, or by thermal fluctuations.[35] Conversely, hard materials, such as metals, oxides, and semiconductors, are typically rigid and brittle, which limits their deformability or resistance to bending, stretching, and impact loading. At the microscopic level, the distinction between soft and hard is described by flexural rigidities and Young's modulus. Young's modulus, an intrinsic property of materials, hardly changes with the geometry of the body. On the contrary, flexural rigidities, an extrinsic property of a material, completely depend on the geometry of the body and can further be tuned to an extent by significantly changing a structure. Rogers et al. reported that the extremely small thickness of NMs, for example, down to 2 nm for silicon, leads to flexural rigidities that can be more than 15 orders of magnitude smaller than those of bulk wafers of the same material.[25] That is, when the minimum lateral dimension is thinned by at least two orders of magnitude, these hard materials can be turned soft and shaped more easily. As a result, even diamond, one of the hardest materials in the nature world, can be rendered soft if it is thin enough.[36] In other words, once hard materials are thinned into membranes as thin as a few nanometers, their behaviors become significantly similar to those of traditional soft matter. In this section, we give a general introduction to inorganic stimuli-responsive materials, along with their growth methods and characteristics.

2.1. VO$_2$ NMs

Vanadium dioxide (VO$_2$) is a strongly correlated electron material with the intriguing metal-insulator phase transition (MIT).[37] It goes through a fully reversible solid-to-solid phase transformation, in which the crystal structure changes from a monoclinic phase to a tetragonal phase at 341 K.[38] Beyond that, the electronic and optical properties suffer a dramatic change via the phase transition, which is widely applied in domain switches,[39] mid-infrared sensors,[40] and stress sensors.[41] Although these changes were first reported nearly 50 years ago, it was not until 2010 when the microscale strain changes of a VO$_2$ film across the phase transition were revealed by Rúa et al.[42] According to their report, the change in area of the crystallographic planes in VO$_2$ parallel to the surface of a micrometer-sized cantilever is capable of producing stress levels that generate significant actuation

Ziao Tian received his B.S. and M.S. degrees from University of Shanghai for Science and Technology and Ph.D. degree in physics from Fudan University. He is an associate professor at Shanghai Institute of Microsystem and Information Technology. Before that, he worked as a postdoctoral researcher in the Department of Material Science at Fudan University. His research is focused on the development of micro/nanotubes fabricated by rolled-up nanotechnology and their functionalization with smart materials.
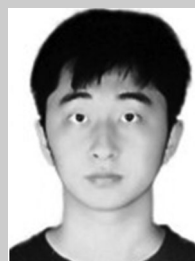
Yang Wang received his B.S. degree in materials physics from Fudan University. He is pursuing his Ph.D. degree in materials science and technology at Fudan University. His research interests include functional devices with smart materials and optical microcavities.

Yongfeng Mei received his B.S. and M.S. degrees in physics from Nanjing University and Ph.D. degree in physics and materials science from City University of Hong Kong. He is a professor in materials chemistry and physics at Fudan University. Before that, he worked as a postdoctoral researcher in the Max Planck Institute for Solid State Research and then led a research group in the Leibniz Institute for Solid State and Materials Research Dresden as a staff scientist. His research interest focuses on the development of novel functional nanomembrane materials and their properties in optics, optoelectronics, flexible electronics, and micro/nanoscale mechanics.

displacements and strain energy densities. These results open up new prospects for actuators in high speed and sensitivity.

Recently, an ultra-thin VO$_2$ NM was reported by Tian et al., who deposited VO$_2$ on a Si substrate with a sacrificial layer, SiO$_2$, and thinned it into an NM by reactive-ion-etching (RIE).[43] The thinning process of the VO$_2$ NM reduces its flexural rigidities, which allows for the formation of 3D nanostructures. Interestingly, the temperature-resistance curves of VO$_2$ films are almost the same, whereas the thicknesses are quite different. Moreover, different from what 2D NMs exhibit on a bulk counterpart, planar VO$_2$ NMs are normally isolated from their environment on both sides, and they should have a larger surface area. VO$_2$ NMs can also possess an improved sensitivity to external environmental stimuli and become more expandable, flexible, or deformable. Therefore, compared with VO$_2$ bulk, less energy is needed to trigger the actuating behavior of the device rolled by VO$_2$ NMs.
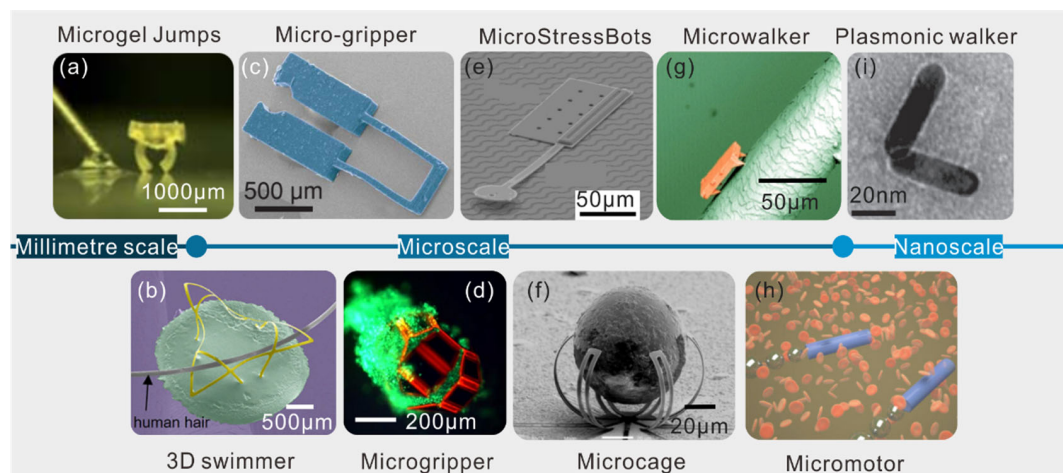
Figure 1. Spectrum of small-scale robot grading from the millimeter scale (left) to nanoscale (right). a) Microgel jumps upon wetting. Reproduced with permission.[27] Copyright 2010, Royal Society of Chemistry; b) FEM images of 3D swimmer suspended by human hairs. Reproduced with permission.[28] Copyright 2017, National Academy of Science; c) An SEM image of a remotely actuated untethered microgripper. Reproduced with permission.[18] Copyright 2014, Wiley-VCH; d) Fluorescent micrograph of viable cells captured using a biochemical trigger to actuate the gripper. Reproduced with permission.[29] Copyright 2009, National Academy of Science; e) SEM image of two MicroStressBots: single arm design. The untethered scratch-driven head provides forward motion, whereas the steering arm actuator determines whether the robot moves forward or turns. Reproduced with permission.[30] Copyright 2006, IEEE; f) SEM image of a microcage capturing a micropolymer ball; Reproduced with permission.[31] Copyright 2011, Wiley-VCH; g) a microwalker walks on the human hairs. Reproduced with permission.[32] Copyright 2015, Wiley-VCH; h) A schematic representation of behavior of microjet engines in reconstituted blood samples. Reproduced with permission.[33] Copyright 2010, American Chemical Society; i) TEM image of the plasmonic walker structures at station. Reproduced with permission.[34] Copyright 2015, Springer Nature.

2.2. SMA NMs

Recently, SMAs have been widely used as smart and functional materials due to their unique ability to recover from large deformations into a predetermined shape under thermal stimuli.[44] After deformation, they can 'remember' their permanent shape via heating, which relies on a reversible diffusionless transformation between two phases: the martensite phase (low temperature) and austenite phase (high temperature), occurring at the transition temperature.[45] Among all SMAs, nitinol (NiTi), a combination of nickel (Ni) and titanium (Ti), has shown superior shape memory characteristics and is the most widely used because of the alloy's outstanding mechanical and shape memory properties, such as an excellent shape-restoring force, high damping capacity, and large transformational strain. An NiTi NM can exhibit a small thermal mass for heating or cooling compared with that of the NiTi bulk, reducing the response time and increasing the operation speed.

The influences of film thickness on the crystallization and shape memory effect of NiTi films have been investigated by several groups.[45,46] In 1990, the NiTi thin film was firstly prepared by Busch et al. using a sputter deposition technique.[47] Afterward, Krulevitch et al. found that with increasing film thickness, NiTi NMs had a lower recoverable stress and higher surface roughness.[48] Kohl et al. deposited an NiTi thin film of 10 μm in thickness by DC magnetron sputtering onto unheated ceramic substrates with a sacrificial layer of Au.[49] For a further decrease in NiTi NMs, Fu et al. investigated surface oxidation and the interfacial diffusion between the film and substrate,[44] finding that the thickness can significantly affect the phase transformation behavior when the film is too thin. The minimum thickness to guarantee an apparent shape memory effect in NiTi NMs is approximately 100 nm.

2.3. Pd NMs

Since the early 1950s, Pd has attracted increasing interest for use in hydrogen-selective reactors,[50] hydrogen separation devices,[51] and hydrogen storage,[52] due to its high solubility of hydrogen over a range of temperatures. Furthermore, with the absorption of hydrogen, such a metallic material experiences a lattice expansion and resistance change because of the phase transition from PdHa to PdHb, which supports possibilities for detection and actuation via hydrogen stimuli.[53] Therefore, multiple structures of Pd materials, ranging from bulk to nanoparticle and membranes, have been applied in sensors for hydrogen absorption. Among these structures, membranes exhibit anisotropic and large biaxial compressive stresses (GPa) with lattice expansion under hydrogen,[54] representing a behavior that is significantly different from that of the bulk material with isotropic expansion, leading to distinct actuation in hydrogen milieu. Thus, membranes based on different thicknesses (from 100 μm to 10 nm), different constructions (dense, metallic, supported, etc.) and different fabrication methods (magnetron sputtering, electroless platting techniques, etc.) have been used in microcantilevers and microtubes for hydrogen detection.

The influence of the thickness of Pd thin films on the mechanical properties under hydrogen stimuli was presented by Stefan et al., in which the compressive stresses increase as the thickness decreases (onset of plastic deformation).[55] As a consequence,

**ADVANCED
SCIENCE NEWS**
www.advancedsciencenews.com

**ADVANCED
INTELLIGENT
SYSTEMS**
Open Access
www.advintellsyst.com

taking advantage of ultra-small thicknesses, Pd NMs can achieve a quick response and high sensitivity to hydrogen, paving the way for ultra-sensitive actuators with low H_2 detection. Recently, Pd NMs used as an actuator for detection were reported by Xu et al.; these materials were deposited on chromium (Cr)/Ti/glass layers with a thickness of 20 nm through e-beam evaporation.[56] This actuator possesses a response time of several seconds and a detection limit down to 1% hydrogen, showing enormous potential for the use of Pd NMs in ultra-sensitive actuators and detectors.
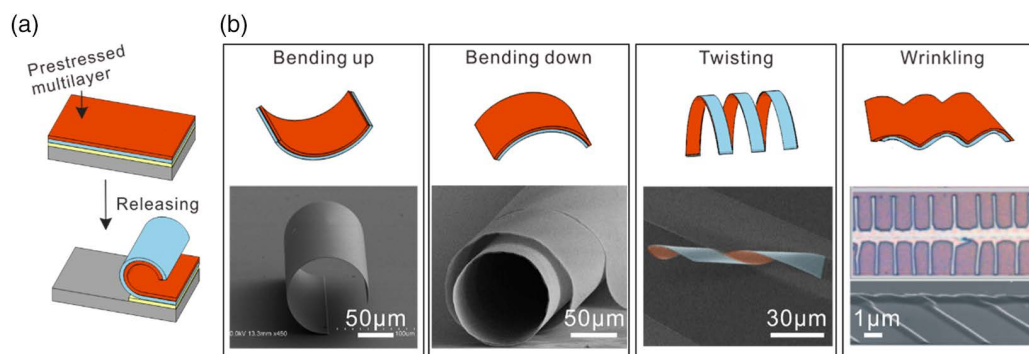
3. Strain-Induced Construction of Mesostructured NMs

3.1. On-Chip Strain Engineering in Inorganic NMs

Strain engineering is the most common method and involves mechanical strain as a manufacturing tool that can be used in the fabrication of various 3D mesostructures by changing certain properties within the NMs. As shown in **Figure 2**a, these 3D structures can be realized from the release of an abundance of inner-strain in a constrained bilayer NMs upon the removal of the constraint of the substrate or its neighboring layers. Exploiting this simple bending phenomenon, various nanostructures, such as tubes, rings, and wrinkles, have been fabricated by the same mechanism, namely, the elastic energy minimization principle.[59] The geometry of a nanostructure is the preferred path to strain energy reduction. The principle of formation of different nanostructures is governed in terms of the geometry of the NM, the elastic properties of the NM, and the strain in the NM. In the bending case, when an NM ribbon is released from the holding substrate, expansion strain along the ribbon axis is restrained by the adjacent layer, where the strain is generated in the opposite direction. As a result, a moment of force is created and leads the bilayer to bend. It is worth noting that different bending directions can be achieved, with the bilayer film bending upward (first column in Figure 2b[57]) or downward (second column in Figure 2b), when a film is stretched or compressed.

If the tensile/compressive strain has a misaligned angle to the ribbon axis, a torsion moment is generated and leads to anisotropic rolling.[60] The leading strain is produced via misfit strains in anisotropic materials with an anisotropic Young's modulus.[61] For instance, Bell et al. manufactured 3D InAs/GaAs nanosprings using AlAs as a sacrificial layer and using a wet etch to release the patterned bilayers.[62] As crystallographic anisotropy dictates that the <100> direction is the preferred roll-up direction, helical ribbons with different pitches and helix angles form depending on the misorientation angle of the ribbon's geometric axes and the bending direction. In addition, in isotropic materials with an isotropic Young's modulus, the leading strain is generated because of the imbalance caused by the etching rates along different sides in this asymmetric shape.[63] According to this principle, Tian et al. discussed a series of helical structures based on different rolling directions that were fabricated by the careful design of photolithography patterns on isotropic nanocrystalline diamond NMs (third column in Figure 2b). Furthermore, this approach has been extended to other materials and material combinations, such as $MoSe_2/Cr$, Cr/Pt, and VO_2.

When the leading strain is not large enough to make NMs bend or roll into a curved structure, the NM wrinkles.[58] A shape diagram of bending/wrinkling based on defined strains inside the constituent layers was presented by Cendula et al.[64] According to this diagram, for a strain gradient $\Delta \varepsilon = 0.20\%$ and an average strain $= \bar{\varepsilon} - 0.36\%$, bending will be favored only until the etching length h is increased to ≈ 700 nm. Beyond this length, the wrinkle becomes the favorable geometry, as it acquires a lower energy than that of the bent structure. When a higher average strain is considered, for example, $= \bar{\varepsilon} - 1.0\%$, the phase boundary curve moves upward, and the wrinkling region is enlarged. In experiments, Mei et al. demonstrated SiGe wrinkle arrays using the internal strain method, where an SiGe NM with a compressive strain is deposited on a sacrificial layer.[58] After being partially released from the substrate by selective etching of the sacrificial layer, the ordered nanochannel network was obtained (fourth column in Figure 2b).

In general, versatility is a prominent advantage of the strain-engineered nanofabrication technique. Varieties of

Figure 2. a) Schematic illustration of the progress of a strain-induced tubular 3D mesostructure. b) Three different classes of nanostructures including tubes, rings, and wrinkles. The first and second column: 3D schematic images and SEM images of a bilayer film bending upward. Reproduced with permission.[57] Copyright 2014, American Chemical Society, and downward, respectively; the third column: a schematic illustration and SEM image of diamond helix; the fourth column: a 3D schematic image (upper panel), an optical microscopy image (middle panel) showing a linear nanochannel network with double-sided branches, and the corresponding SEM image (bird view) of a single-sided linear nanochannel network (lower panel). Reproduced with permission.[58] Copyright 2010, Elsevier.

nanomechanical architectures can be designed with different materials, including semiconductors, metals, and insulators as well as active materials. A high degree of control can also be achieved in principle, as the size and shape can be tuned over a wide range by choosing different combinations of materials, varying film dimensions, and applying external forces. Therefore, this approach makes it possible for the parallel mass production of identical or different nanostructures.

3.2. External Strain Tuning for 3D Mesostructures

In addition to the intrinsic strain-induced assembly, the external stress enables the transformation from 2D sheets to 3D mesostructures on the microscopic scale due to the flexibility of materials, similar to origami arts.[65] Attributed to the microscale, capillary forces become considerable compared with bulk forces, resulting in possibilities to tune structures by controlling the surface tension. The interaction between capillary and elastic forces generates the distinguished deflection of planar objects, which drives the folding assembly from submillimeter to micrometers. The actuating approaches of capillarity implemented in sophisticated 3D structures involve wet droplets[66] and melting hinges,[67] whereas the critical parameters of 2D sheets are deduced from the balance between interfacial and elastic bending energies. For example, Py et al. demonstrated the spontaneous wrapping of polydimethylsiloxane (PDMS) membranes into the spherical encapsulation, the cubic encapsulation, and the triangular mode twofold, illustrating the reliability of capillary force-induced assembly folding. The authors also found that the critical length scale of encapsulation was dependent on thickness as $h^{3/2}$, suggesting an optimized scale for the fabrication minima of 3D mesostructures.[66]

Apart from the folding derived from capillary forces, the external stress also causes other origami approaches such as buckling, which relies on deformable substrates to provide forces. Xu et al. conceptually proposed a universal assembly strategy to fabricate inaccessible classes of 3D mesostructures by relaxing strain in a prestretched elastomeric substrate while imparting forces such as bonding at selective locations of 2D precursor structures.[68] While the substrate recovers from uniaxial stretching, large compressive forces induce the planar pattern having an out-of-plane deformation, and the bonding sites with different works of adhesion lead to the precursor selectively lifting off. Utilizing such a promising method, the researchers manufactured more than 40 architectures, ranging from helices and flowers to frameworks, using different planar patterns, compressive strain, and bonding sites. The assembly buckling benefiting from a high compatibility is also capable of electronic devices,[69] wearable devices, and plasmonic structures.[70] The strategy of buckling was further reported by Fu et al. for reconfigurable devices based on multistable mechanics. The authors applied selected releasing sequences and pattern designs to make the elastomer platforms deform in different time sequences, inducing different 3D structures with the same planar configurations as those provided by multistability.[71] As different loading paths were adopted in a set of reconfigurable geometries with different materials, this strategy can be applied in radiofrequency circuits and antennas, indicating the potential of reconfigurable devices, which will be possible to use in actuators and robots.
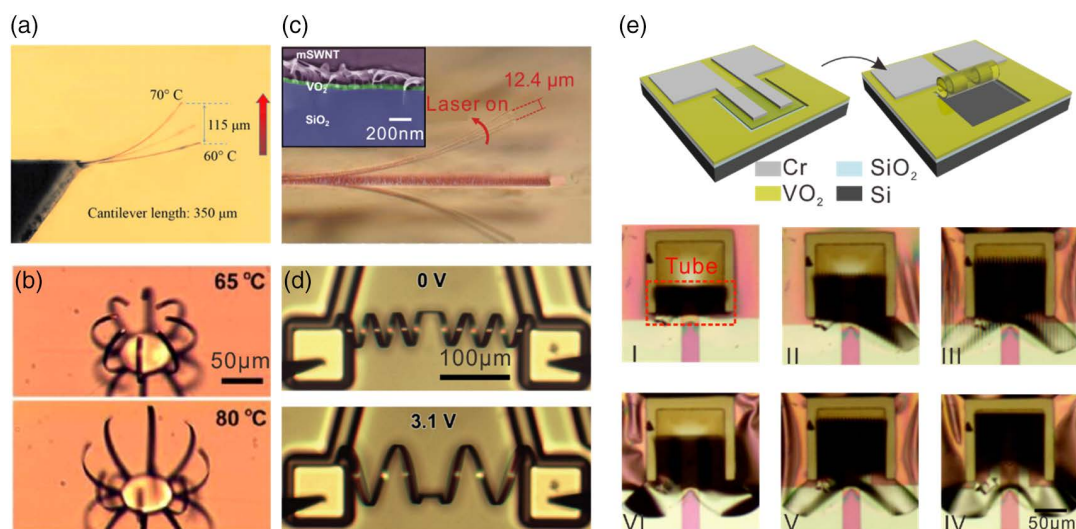
4. Applications

4.1. VO$_2$ Actuation

In the transition process of VO$_2$ from an insulator phase to a metal phase, compressive strain is produced by a phase transition that can be applied in actuators driven by heat.[72] As obtained from experimental curvature measurements, the strains are approximately 2% and 1% when the phase transits from M_2 to R and M_1 to R, respectively.[73] In 2010, using VO$_2$ as a micromechanical actuator was first reported by Nelson Sepúlveda et al.[42] A maximum curvature change of $2000 \, m^{-1}$ in a bimorph cantilever (shown in **Figure 3**a) composed of polycrystalline VO$_2$ film deposited on single-crystal Si was observed through the narrow temperature range of the IMT to exhibit a maximum rate of $485 \, m^{-1}$ per degree. The authors also suggested that reducing the application dimension in actuator devices may contribute to higher operational frequencies. To enhance the bending curvature resulting from a targeted temperature change, Liu et al. investigated VO$_2$/Cr bimorph microactuators at the sub-100 μm length scale, as shown in Figure 3b, where the microcantilever produces a change in curvature of approximately $20\,000 \, m^{-1}$ at the phase transition temperature.[74] Moreover, the authors claimed that the work density of these devices is comparable to that of SMAs, which is over an order of magnitude higher than that of inorganic materials and electrostrictive polymers and over three orders of magnitude higher than that of human muscles ($\approx 0.008 \, J \, cm^{-3}$).

As an additional stimulus, laser light provides a remote and wireless way to trigger VO$_2$-based microactuators. By incorporating carbon nanotubes (CNTs) into VO$_2$ bilayer actuators, flexible, all-inorganic actuators based on the bimorph structure were designed by Ma et al.[77] CNTs can improve the effectiveness of absorbing light and reduce the photothermal energy required for actuation. Thus, the drastic, reversible phase transition of VO$_2$ drives the actuators to deliver a giant amplitude, fast response up to $\approx 100 \, Hz$, and long lifetime of more than 1×10^6 actuation cycles. As shown in Figure 3c, a high-performance photothermal microactuator was reported by Wang et al. in 2017.[75] The inset in Figure 3c shows that a single-walled carbon nanotube (SWNT) layer, with a thickness of 100 nm, was coated on a VO$_2$ NM. The presented VO$_2$/SWNT-based microphotoactuators show displacements that are dependent on the wavelength of the light incident on the device while maintaining an excellent performance in terms of a large displacement, low power consumption, large energy density, and fast response. The results indicated that the VO$_2$ can not only be actuated thermally with laser light but also be stimulated to a higher actuation bandwidth than that achieved via conduction heating actuation.

Apart from thermal and photothermal actuations, electrothermal actuation has also attracted attention because it can be controlled precisely in circuits. For example, an electrotriggered torsional muscle was prepared by Liu et al. through the release of a "V"-shaped Cr/VO$_2$ bimorph structure.[76] Figure 3d shows a dual coil rotating to its maximum amplitude under an input voltage of 3.1 V, where the input power is only $\approx 3 \, mW$. As the driving voltage slowly varies, the coil switches between a high-resistance state corresponding to the insulating phase of VO$_2$ and a low-resistance one corresponding to the metallic phase.

**ADVANCED
SCIENCE NEWS**
www.advancedsciencenews.com

**ADVANCED
INTELLIGENT
SYSTEMS**
Open Access
www.advintellsyst.com

Figure 3. a) Multiple exposures picture of a VO$_2$-coated silicon cantilever during heating. The temperature was measured with a thermocouple attached to the chip. Reproduced with permission.[42] Copyright 2010, American Institute of Physics. b) A microactuator with a "palm" structure, showing the fingers closed at 65 °C and open at 80 °C. The scale bar is 50 µm. Reproduced with permission.[74] Copyright 2012, American Chemical Society. c) The light response of the VO$_2$/mSWNT actuator for pulses from a 660 nm laser. The inset shows an SEM image of a cross section of the VO$_2$/mSWNT actuators. Reproduced with permission.[75] Copyright 2017, Science. d) The geometry of a dual coil actuated at 0 and 3.1 V. Scale bar is 100 µm. Reproduced with permission.[76] Copyright 2014, Wiley-VCH. e) Upper panel: a schematic of a Cr/VO$_2$ bimorph structure obtained by selective etching of the SiO$_2$ sacrificial layer. Lower panel: optical images of the rotation of the tube at various temperatures in a heating–cooling cycle. Reproduced with permission.[43] Copyright 2018, American Chemical Society. The dark part represents the bimorph, rolling into tube (red rectangle) at a low temperature and flattening into a quadrate NM.
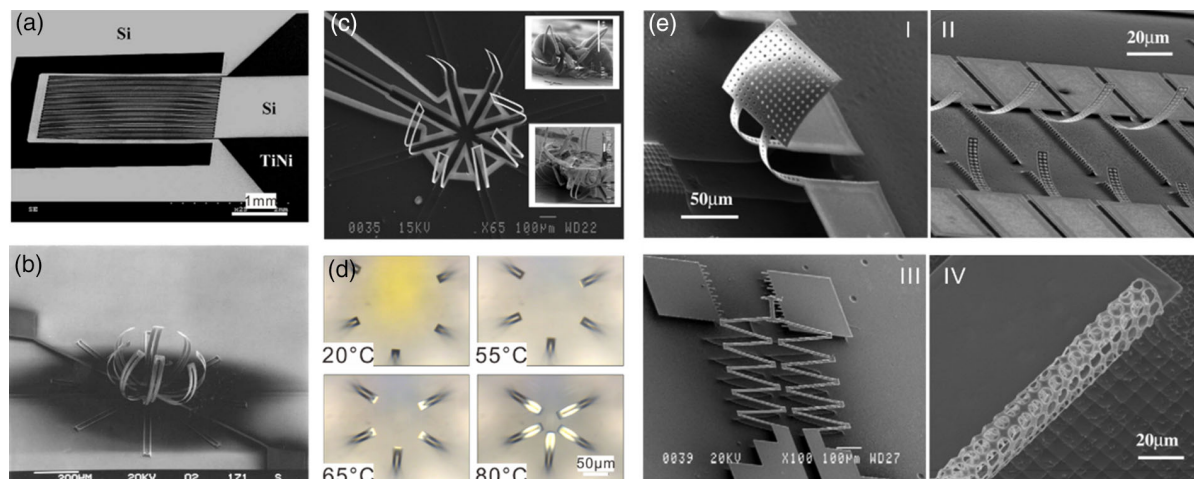
A reversible torsional motion for greater than 1 million cycles without degradation was also demonstrated, along with a superior rotational speed of up to ≈200 000 rpm, an amplitude of 500° per mm length, and a power density of up to ≈39 kW kg^{-1}.

Recently, Tian et al. reported a bimorph established on the basis of an ultra-thin VO$_2$ NM (Figure 3e), which was constructed as a microtubular structure due to the low bending stiffness of the bilayer NM system.[43] The rolled-up tubular structure redistributes the strain inside the bilayer NM, resulting in an additional compressive strain in the outer layer consisting of VO$_2$, which can be tuned via the deposition thickness of the structural layer. On the one hand, through this strain engineering, the MIT voltage and temperature become lower by controlling the curvature of the tube. On the other hand, compared to the properties of a thick film, the low MIT voltage and hysteresis width are attributed to the ultra-thin crystals of VO$_2$. Therefore, a tubular microactuator with strain compensation, a low energy requirement, and a large displacement was fabricated with different triggering temperatures. Lower Figure 3e shows the actuating behavior of a VO$_2$/Cr bimorph device dependent on the temperature variation. Additionally, the curvature of the VO$_2$/Cr bimorph, with a change of 4.5×10^4 m^{-1} or more, is observed to be considerably better than that of existing VO$_2$ microactuators.

4.2. TiNi Actuation

As TiNi films can proved a high density (up to 10 J cm^{-3}) and large displacement in actuating behavior, many microactuators, such as grippers, helices, cantilevers, wrappers, and positioners, have been realized. Additionally, the good biocompatibility of TiNi is promising for biological applications. In recent years,

microactuators based on TiNi thin films have made considerable progress. An integrated TiNi/Si cantilever with a reverse actuating behavior is the most popular structure for out-of-plane bending, as shown in **Figure 4**a,[78] where the patterned TiNi is deposited on Si cantilevers as electrodes. When a voltage is applied to the surface of TiNi, a small current passes through the TiNi NM and allows it to heat. Due to the shape memory effects of TiNi films, a gripping force is generated and thus bends the cantilever upward. To form a gripping movement, an electro-triggered microwrapper is designed by the in-plane mode, in which the deformable eight arms (shown in Figure 4b) lay within a plane through a compliant structure design.[79] A fairly large electropower of ≈400 mW is required to open the microwrapper, allowing the heat to transfer to the silicon substrate from the microwrapper. Fu et al. designed a microcage based on free-standing TiNiCu films leading to better thermal isolation between the heated microactuator and substrate, whereby significant displacements are clearly observed as the SMA heats up through the transition temperature, for input powers between 1.5 and 5 mW. Figure 4c shows a TiNiCu up-bending microcage structure and examples of capturing of an ant (top) and an aphid (bottom),[80] whereas another TiNi/diamond-like-carbon (DLC) microcage was designed for biological applications, as shown in Figure 4d.[31] Strain-free TiNi is deposited on the DLC under compressive strain, and after releasing from the substrate, the fingers bend up but do not meet each other. As the temperature increases above the start of the austenite transformation temperature (≈50–60 °C), martensite changes into austenite, causing the closing of the microcage and the capturing of an object. When the heating stops, the system starts to cool to room temperature, and NiTi suffers from the reverse transition so that the

1900092 (6 of 12)

**ADVANCED
SCIENCE NEWS**

www.advancedsciencenews.com

**ADVANCED
INTELLIGENT
SYSTEMS**
Open Access

www.advintellsyst.com

Figure 4. a) The patterned TiNi electrodes on a silicon cantilever. Reproduced with permission.[78] Copyright 2004, Elsevier. b) An SEM image of NiTi microwrapper. Reproduced with permission.[79] Copyright 2001, Elsevier. c) A TiNiCu microcage structure bending up and examples of capturing an ant (upper) and an aphid (lower). Reproduced with permission.[80] Copyright 2009, Inderscience. d) Optical microscopy images showing the closing of a five-finger microcage during heating (during cooling the process is reversed; beam length: 150 μm): 20, 55, 65, and 80 °C. Reproduced with permission.[31] Copyright 2011, Wiley-VCH. e) Free-standing TiNiCu structures: I. a cantilever, II. multilength cantilevers, III. microsprings, and IV. a microstent. Reproduced with permission.[80] Copyright 2009, Inderscience.

fingers unfold into opened microcages again. More examples of released structures (I. cantilever mirror, II. multilength cantilever, III. microspring, and IV. microstent) actuated by heating/cooling through the two-way shape memory effect are shown in Figure 4e.[80]
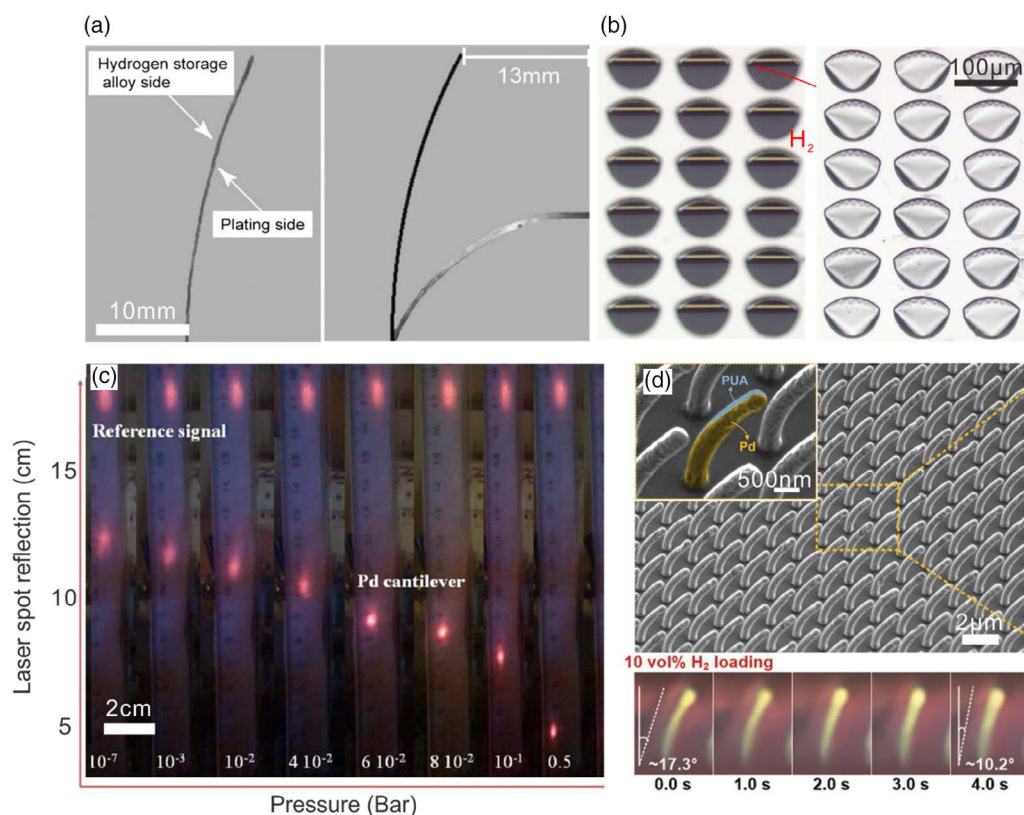
4.3. Pd Actuation

On account of the lattice expansion of Pd during the phase transition with hydrogen absorption, diverse structures have been fabricated to detect hydrogen gas by the actuation behaviors, ranging from microribbons, microrolls, and microcantilevers to nanofibers. One microribbon actuator driven by hydrogenation was reported by Mizumoto et al., and it consisted of Pd–Ni alloys (left side) and Cu-plating (right side); the device possesses a distinct bending behavior initiated by hydrogen absorption that consists of a 7.5 mm displacement in 6 min hydrogen stimuli (first cycle) and then recovery in 45 min (**Figure 5**a).[81] However, another kind of large arrayed microrolls for hydrogen detection was designed by Xu et al., as shown in Figure 5b,[56] and was fabricated with NMs by strain engineering and origami technology. Based on their intrinsic strain gradient, these NMs were patterned and then rolled up via self-assembly through etching of the scarified layer. In the hydrogen milieu, the microroll changes from a curved state to a planar state under the volume expansion of the Pd layer with a response time of several seconds, which leads to the enhanced macroscopic visual detection of hydrogen that benefits from the large array of ultra-thin membranes. As shown in Figure 5c, Ollagnier et al. prepared a microcantilever, with a 30 nm Pd layer coated on bare silicon, to detect hydrogen pressure.[82] The different hydrogen pressures were deduced from the changing position of a laser spot reflected from a bending microcantilever. Furthermore, Han et al. reported Pd-based Janus nanofibers coated with different

materials on two sides: one side was Pd and the other was a polymer (polyurethane acrylate, PUA), which exhibits a response behavior to hydrogen in eye-readable sensors.[83] Taking inspiration from the insect sensilla, these nanofibers generate a bending angle under air because of the slant of the Ar-ion-beam irradiation being incorporated in the Pd deposition, which decreases upon hydrogen exposure. Figure 5d shows an array of nanofibers amplifying the surface area for sensing and the dynamic changes in the bending angle from 17.3° to 10.2° within 4 s, indicating the high detection sensitivity toward hydrogen, that support eye-readable sensors from the structural changes of the large array.

4.4. Hybrid Actuation

To construct more complex functional devices, the hybrid system and structure composed by different materials across length scales are emerging. Recent advances point to the feasibility of truly structured integration of inorganic NMs with organic responsive materials. For example, polymers are typically isotropic materials that undergo only uniform volumetric expansion and contraction in response to one or sometimes a few stimuli, such as temperature,[10] pH,[11] and enzymes.[84] As a result, combined with stiffer components, its swelling can be restricted in certain positions or directions, thus defining the distribution of strains in the material and therefore the shape adopted. Moreover, polymer has attracted wide attention in biomedical application due to its good biocompatibility.[10] Hybrid microgrippers with alternating rigid segments and flexible hinges are shown in **Figure 6**a.[84] The rigid segments of gripper consisting of Cr, Ni, and Au were deposited and patterned by lift-off metallization and electrodeposition. Ni is incorporated to allow for remote magnetic manipulaton. Aqueous biopolymer was dispensed onto the features and patterned into hinge-like shapes. The flexible hinges are initially flat and curved only

Figure 5. Pd actuation for hydrogen detectors. a) A ribbon, with an alloy and Cu plating, having a large responsive displacement under hydrogen stimuli. Reproduced with permission.[81] Copyright 2009, Elsevier. b) Microrolls with Pd/Cr/Ti NMs generating an enhanced macroscopic visual detection with hydrogen milieu due to the deformation from rolled-up structures to planar sheets. Reproduced with permission.[56] Copyright 2018, Science. c) A Pd microcantilever for detecting hydrogen pressure by measuring the laser location reflected from the cantilever. Reproduced with permission.[82] Copyright 2013, Elsevier. d) Nanofiber arrays coated with Pd as eye-readable hydrogen sensors, which are based on the change in the bending angle. Reproduced with permission.[83] Copyright 2017, Wiley-VCH.
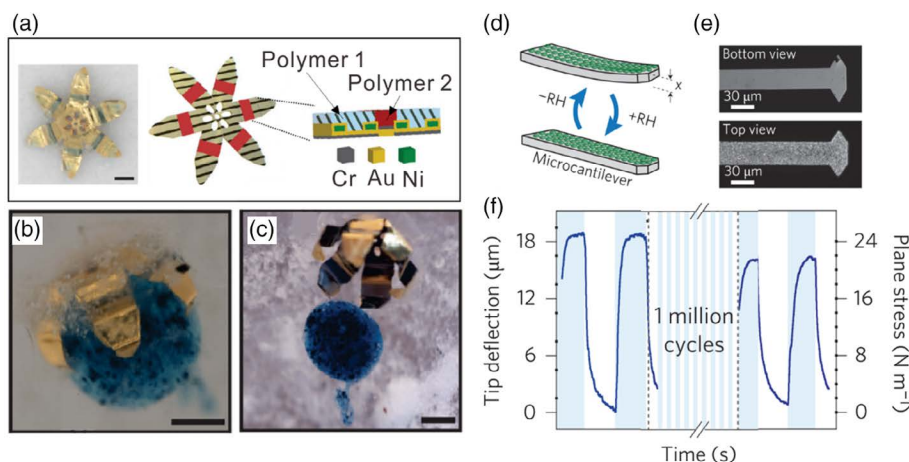
Figure 6. a) Optical and schematic image of hybrid gripper with integrated polymer layers that can close and reopen on exposure to enzymes. b) Hybrid closed gripper in response to cellulase to retrieve a 700 µm alginate bead outside the model. After placing the gripper in the duodenum, we guided it deep into the liver with a magnetic stylus. c) Opened hybrid gripper in response to collagenase. Scale bar is 200 µm in (b) and (c). a–c) Reproduced with permission.[84] Copyright 2010, American Chemical Society. d) Spores placed on silicon microcantilevers. e) Optical micrographs of the bottom (upper) and top (lower) of a silicon AFM cantilever. f) Displacement of the cantilever tip and the corresponding surface stresses in response to changing relative humidity, recorded before and after 1 million cycles between 15% and 85% relative humidity. d–f) Reproduced with permission.[85] Copyright 2014, Nature Publishing Group.

**ADVANCED
SCIENCE NEWS**

www.advancedsciencenews.com

**ADVANCED
INTELLIGENT
SYSTEMS**
Open Access

www.advintellsyst.com

on exposure to the appropriate enzyme. In Figure 6b, the gripper is close using a cellulase trigger, and then is able to move with the bead securely in its grasp using a magnetic stylus. Subsequently, the bead is released using a collagenase trigger, as shown in Figure 6c. Another example is shown in Figure 6d–f, where a hybrid spores-microcantilever response to water gradients is exhibited.[85] The differential strain exerted by the spores caused a change in the curvature of the microcantilevers, as shown in Figure 6d. An AFM (shown in Figure 6e) is used to characterize the cantilever deformations by reflecting the laser from the uncoated surface. Excellent reversibility of hybrid microcantilever and a relatively fast response to variations in water potential are shown in Figure 6f. This hybrid actuation shows great promise in bringing further advancement well beyond field of conventional responsive materials.

4.5. SNMs for Reconfigurable Robots

Inspired by the plants in nature demonstrating a good shape-changing ability to adapt to complex and volatile environments, recent efforts have been focused on creating deformable and reconfigurable robots to meet the need of complicated tasks, such as noninvasive microsurgery, diagnosis, and therapy.[86] To this end, small-scale multifarious reconfigurable robots based on smart membranes have been created. For instance, Huang et al. presented a magnetically powered microrobot with a reconfigurable shape by patterning multiple hydrogel layers, which generated a stiffness gradient within the hydrogel, thus triggering an initiate self-folding behavior.[5] A swimming motion can be controlled by oscillating magnetic fields when magnetic nanoparticles were embedded in the hydrogel. Moreover, the

shape can be controlled using both local heating and optothermal by near-infrared (NIR), as shown in **Figure 7**a.[5] The tubular hydrogel shows a long slender shape as a low temperature (25 °C) is achieved along the strain gradient, whereas the tubular head unfolds and then refolds to a short stumpy shape when the robot is irradiated by an NIR laser. The significantly different forward speeds of the long slender form and of the short stumpy form are shown in the lower panel of Figure 7a. Recently, an actively reconfigurable robot with a several degrees of freedom was introduced by Kim et al., and the device can crawl, roll, catch fast-moving objects, and transport a pharmaceutical dose.[87] A 2D planar hexapedal membrane incorporating ferromagnetic neodymium–iron–boron microparticles and silica nanoparticles was fabricated via direct writing. The membrane can rapidly transform into a complex 3D shape when exposed to applied magnetic fields of 200 mT, as a result of the programmed ferromagnetic domains (shown in Figure 7b).[87] Although the devices produced by this method are not small enough, the shape reconfiguration of constructs via external stimuli offers a novel and highly promising path for generating next-generation robots.

5. Conclusion and Outlook

As a new member of NMs, with a thickness in the range of one to a few hundred nanometers, SNMs provide an excellent motivation for expanding activities in the small-scale robotic field. Together with strain engineering for deterministic assembly, various smart actuators maintaining excellent performance in terms of large displacement, low power consumption, large energy density, and fast response have been manufactured.
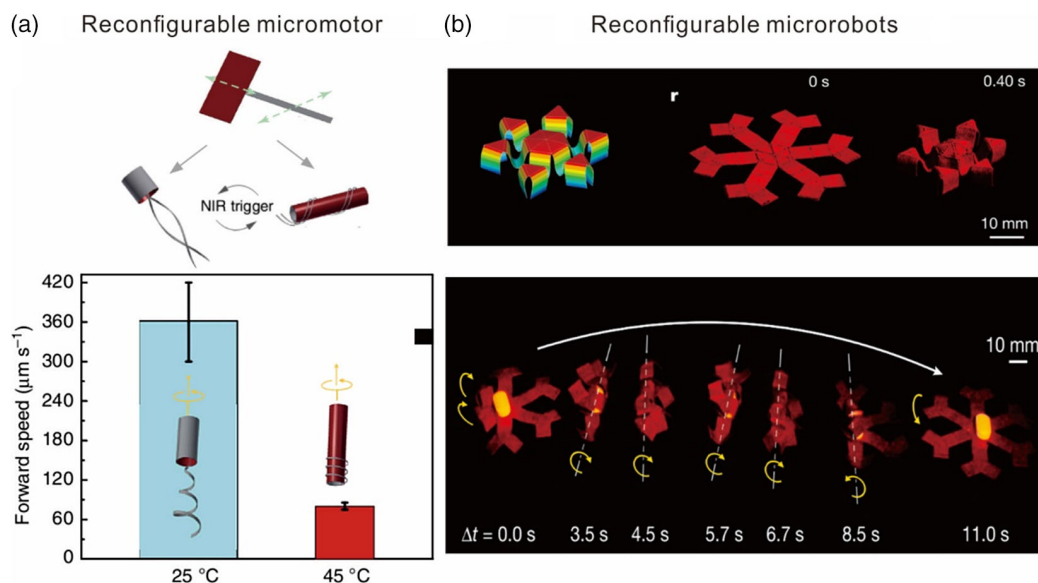
Figure 7. a) Upper panel: the soft micromachine can be programmed to transform its shape when exposed to external NIR heating; lower panel: the forward speed of the micromachine at different morphological states driven with the same strength and frequency of rotating magnetic field. Reproduced with permission.[5] Copyright 2016, Nature Publishing Group. b) Upper panel: an LMC-made octopus transforms from a 2D shape into a 3D shape; the scale bar is 2 cm. Middle panel: hexapedal structures with programmed ferromagnetic domains demonstrating complex shape changes under applied magnetic fields. Lower panel: a hexapedal structure wrapping an oblong pharmaceutical pill and carrying the pill using rolling-based locomotion. Reproduced with permission.[87] Copyright 2018, Nature Publishing Group.

1900092 (9 of 12)

Table 1. Three stimuli-responsive materials applied in actuators and robotics.

Materials	Energy density	Composition of robotics/actuators	Length scale	Responsive performance	Reference
Vanadium dioxide (VO_2)	7–28 $J\,cm^{-3}$,[74,77]	VO_2/Cr cantilevers	nm–μm	Bending	[74]
	0.8 $J\,cm^{-3}$ with a temperature window of 15 °C[88]			Response time: 0.13 ms	
		VO_2/Cr coils	nm–μm	Rotation	[76]
				Response time: 0.34 ms	
		VO_2/CNT cantilevers	μm–mm	Bending	[77]
				Response time: 12.5 ms	
Titanium (Ti)/Nickel (Ni) shape memory alloys	≈6 $J\,cm^{-3}$[89]	TiNiCu structures	μm–mm	Bending	[80]
				Response time: 10 ms	
Palladium (Pd)	≈4 $J\,cm^{-3}$[90]	Ti/Cr/Pd microrolls	nm–μm	Rolling	[56]
				Response time: 3.4 s	
		Janus Pd/PUA nanofibers	nm–μm	Bending	[83]
				Response time: 5.1 s	

In this review, the properties of three typical SNMs (VO_2, TiNi, and Pd) and examples of SNM devices are summarized. Some properties and applications of these materials are shown in **Table 1**. All of three materials have high energy densities (VO_2: 7–28 $J\,cm^{-3}$, TiNi: ≈6 $J\,cm^{-3}$, Pd: ≈4 $J\,cm^{-3}$), leading to large potential applied in actuator and robotic devices with small scales (nanometers to micrometers) and quick response time (milliseconds), which were confirmed in various structures (cantilevers, coils, rolls, etc.). Different from their bulk counterparts, these planar NMs are normally isolated from their environment on both sides, and they should possess a larger surface area, thus providing improved sensitivity to external environmental stimuli. In addition, because of their good elasticity, light weight, high deformability, and high transparency, NMs can exhibit a great shape-changing capability and offer a strong impetus for the development of soft robots, artificial muscles, biomimetic devices, and beyond. The NMs can also achieve a combination of attributes, thereby enhancing a high response efficiency, material processability, and long-term stability. The free-standing NMs can form a bridge between material property and architecture geometry for materials research, a topic that may hint at applying the 2D concept to conventional material platforms in the future.

Although advanced SNMs have been applied in the field of actuators to realize reconfigurable morphing, autonomous sensing, and actuating, there are many challenges to fabricating small-scale robots with SNMs. The primary challenge rests with the design and fabrication of an SNM robot body that matches its structure to a given task. The rolling and folding method leaves little opportunity to fine-tune structures or control the stages of hierarchical development, let alone to rationally design arbitrary architectures. We need to seek for precise control over the directions of every roll and fold. Furthermore, as the complexity of the robots increases, the number of folds and thus the coordination of each of folding are required. Another challenge is the operation of robots with high speed and precision. Although many micromanipulation systems exhibit substantial infrastructure, a general micromanufacturing approach with an emphasis on biocompatibility

and integration is still missing. When these requirements are met, a shape-changing, self-healing, and evolving small-scale robot can be reached.

Acknowledgements

Conflict of Interest

The authors declare no conflict of interest.

Keywords

[1] a) W. Hu, G. Z. Lum, M. Mastrangeli, M. Sitti, *Nature* **2018**, *554*, 81; b) L. Hines, K. Petersen, G. Z. Lum, M. Sitti, *Adv. Mater.* **2017**, *29*, 1603483; c) R. Wood, C. Walsh, *Sci. Transl. Med.* **2013**, *5*, 210ed19; d) Z. Zhakypov, K. Mori, K. Hosoda, J. Paik, *Nature* **2019**, *571*, 381; e) M. Sitti, H. Ceylan, W. Hu, J. Giltinan, M. Turan, S. Yim, E. Diller, *Proc. IEEE* **2015**, *103*, 205.

[2] a) B. Xu, B. Zhang, L. Wang, G. Huang, Y. Mei, *Adv. Funct. Mater.* **2018**, *28*, 1705872; b) J. Li, S. Thamphiwatana, W. Liu, B. Esteban-Fernández De Ávila, P. Angsantikul, E. Sandraz, J. Wang, T. Xu, F. Soto, V. Ramez, X. Wang, W. Gao, L. Zhang, J. Wang, *ACS Nano* **2016**, *10*, 9536; c) V. Magdanz, S. Sanchez, O. G. Schmidt, *Adv. Mater.* **2013**, *25*, 6581; d) B. J. Nelson, I. K. Kaliakatsos, J. J. Abbott, *Annu. Rev. Biomed. Eng.* **2010**, *12*, 55.

[3] R. Wood, C. Walsh, *Sci. Transl. Med.* **2013**, *5*, 210ed19.

[4] G. Yang, J. Bellingham, H. Choset, P. Dario, P. Fischer, T. Fukuda, N. Jacobstein, B. Nelson, M. Veloso, J. Berg, *Sci. Robot.* **2016**, *1*, eaal2099.

[5] H. Huang, M. S. Sakar, A. J. Petruska, S. Pane, B. J. Nelson, *Nat. Commun.* **2016**, *7*, 12263.

[6] S. Kobatake, S. Takami, H. Muto, T. Ishikawa, M. Irie, *Nature* **2007**, *446*, 778.

[7] H. Zeng, P. Wasylczyk, D. S. Wiersma, A. Priimagi, *Adv. Mater.* **2017**, *30*, 1703554.

[8] E. A. M. R. A. Sydney Gladman, *Nat. Mater.* **2016**, *15*, 413.

[9] a) J. J. Wie, M. R. Shankar, T. J. White, *Nat. Commun.* **2016**, *7*, 13260; b) O. M. Wani, H. Zeng, A. Priimagi, *Nat. Commun.* **2017**, *8*, 15546.

[10] a) S. Kumar, M. D. Pickett, J. P. Strachan, G. Gibson, Y. Nishi, R. S. Williams, *Adv. Mater.* **2013**, *25*, 6128; b) E. Gultepe, J. S. Randhawa, S. Kadam, S. Yamanaka, F. M. Selaru, E. J. Shin, A. N. Kalloo, D. H. Gracias, *Adv. Mater.* **2013**, *25*, 514.

[11] C. Ma, W. Lu, X. Yang, J. He, X. Le, L. Wang, J. Zhang, M. J. Serpe, Y. Huang, T. Chen, *Adv. Funct. Mater.* **2018**, *28*, 1704568.

[12] J. S. Kahn, Y. Hu, I. Willner, *Acc. Chem. Res.* **2017**, *50*, 680.

[13] D. Han, C. Farino, C. Yang, T. Scott, D. Browe, W. Choi, J. W. Freeman, H. Lee, *ACS Appl. Mater. Interfaces* **2018**, *10*, 17512.

[14] M. Acerce, E. A. An, M. Chhowalla, *Nature* **2017**, *549*, 307.

[15] a) J. Kim, S. E. Chung, S. Choi, H. Lee, J. Kim, S. Kwon, *Nat. Mater.* **2011**, *10*, 747; b) J. C. Breger, C. Yoon, R. Xiao, H. R. Kwag, M. O. Wang, J. P. Fisher, T. D. Nguyen, D. H. Gracias, *ACS Appl. Mater. Interfaces* **2015**, *7*, 3398.

[16] X. Qian, Q. Chen, Y. Yang, Y. Xu, Z. Li, Z. Wang, Y. Wu, Y. Wei, Y. Ji, *Adv. Mater.* **2018**, *30*, 1801103.

[17] S. Palagi, A. G. Mark, S. Y. Reigh, K. Melde, T. Qiu, H. Zeng, C. Parmeggiani, D. Martella, A. Sanchez-Castillo, N. Kapernaum, F. Giesselmann, D. S. Wiersma, E. Lauga, P. Fischer, *Nat. Mater.* **2016**, *15*, 647.

[18] E. Diller, M. Sitti, *Adv. Funct. Mater.* **2014**, *24*, 4397.

[19] E. Jager, E. Smela, O. Inganas, *Science* **2000**, *290*, 1540.

[20] X. Lu, S. Guo, X. Tong, H. Xia, Y. Zhao, *Adv. Mater.* **2017**, *29*, 1606467.

[21] H. Arazoe, D. Miyajima, K. Akaike, F. Araoka, E. Sato, T. Hikima, M. Kawamoto, T. Aida, *Nat. Mater.* **2016**, *15*, 1084.

[22] T. Taniguchi, H. Sugiyama, H. Uekusa, M. Shiro, T. Asahi, H. Koshima, *Nat. Commun.* **2018**, *9*, 538.

[23] T. J. White, D. J. Broer, *Nat. Mater.* **2015**, *14*, 1087.

[24] Y. Zhang, F. Zhang, Z. Yan, Q. Ma, X. Li, Y. Huang, J. A. Rogers, *Nat. Rev. Mater.* **2017**, *2*, 17019.

[25] J. A. Rogers, M. G. Lagally, R. G. Nuzzo, *Nature* **2011**, *477*, 45.

[26] F. Cavallo, M. G. Lagally, *Soft Matter* **2010**, *6*, 439.

[27] H. Lee, C. Xia, N. X. Fang, *Soft Matter* **2010**, *6*, 4342.

[28] Z. Yan, M. Han, Y. Shi, A. Badea, Y. Yang, A. Kulkarni, E. Hanson, M. E. Kandel, X. Wen, F. Zhang, Y. Luo, Q. Lin, H. Zhang, X. Guo, Y. Huang, K. Nan, S. Jia, A. W. Oraham, M. B. Mevis, J. Lim, X. Guo, M. Gao, W. Ryu, K. J. Yu, B. G. Nicolau, A. Petronico, S. S. Rubakhin, J. Lou, P. M. Ajayan, K. Thornton, et al., *Proc. Natl. Acad. Sci. USA* **2017**, *45*, E9455.

[29] T. G. Leong, C. L. Randall, B. R. Benson, N. Bassik, G. M. Stern, D. H. Gracias, *Proc. Natl. Acad. Sci. USA* **2009**, *106*, 703.

[30] B. R. Donald, C. G. Levey, C. D. McGray, I. Paprotny, D. Rus, *J. Microelectromech. Syst.* **2006**, *15*, 1.

[31] a) C. Wu, H. Wei, B. Ning, Y. Xie, *Adv. Mater.* **2010**, *22*, 1972; b) B. Hu, Y. Zhang, W. Chen, C. Xu, Z. L. Wang, *Adv. Mater.* **2011**, *23*, 3536.

[32] H. Zeng, P. Wasylczyk, C. Parmeggiani, D. Martella, M. Burresi, D. S. Wiersma, *Adv. Mater.* **2015**, *26*, 3883.

[33] a) J. Cao, Y. Gu, W. Fan, L. Q. Chen, D. F. Ogletree, K. Chen, N. Tamura, M. Kunz, C. Barrett, J. Seidel, J. Wu, *Nano Lett.* **2010**,
10, 2667; b) Y. Ke, S. Wang, G. Liu, M. Li, T. J. White, Y. Long, *Small* **2018**, *14*, 1802025.

[34] C. Zhou, X. Duan, N. Liu, *Nat. Commun.* **2015**, *6*, 8102.

[35] J. D. Meglio, D. Quéré, P. D. Gennes, *Langmuir* **1991**, *7*, 335.

[36] Z. Tian, L. Zhang, Y. Fang, B. Xu, S. Tang, N. Hu, Z. An, Z. Chen, Y. Mei, *Adv. Mater.* **2017**, *29*, 1604572.

[37] M. Liu, H. Y. Hwang, H. Tao, A. C. Strikwerda, K. Fan, G. R. Keiser, A. J. Sternbach, K. G. West, S. Kittiwatanakul, J. Lu, S. A. Wolf, F. G. Omenetto, X. Zhang, K. A. Nelson, R. D. Averitt, *Nature* **2012**, *487*, 345.

[38] a) A. Ishida, M. Sato, *Acta Mater.* **2003**, *51*, 5571; b) D. Wan, K. Komvopoulos, *J. Mater. Res.* **2005**, *20*, 1606.

[39] C. Wu, H. Wei, B. Ning, Y. Xie, *Adv. Mater.* **2010**, *22*, 1972.

[40] Z. Li, Z. Hu, J. Peng, C. Wu, Y. Yang, F. Feng, P. Gao, J. Yang, Y. Xie, *Adv. Funct. Mater.* **2014**, *24*, 1821.

[41] J. Cao, Y. Gu, W. Fan, L. Q. Chen, D. F. Ogletree, K. Chen, N. Tamura, M. Kunz, C. Barrett, J. Seidel, J. Wu, *Nano Lett.* **2010**, *10*, 2667.

[42] A. Rúa, F. E. Fernandez, N. Sepulveda, *J. Appl. Phys.* **2010**, *107*, 74506.

[43] Z. Tian, B. Xu, B. Hsu, L. Stan, Z. Yang, Y. Mei, *Nano Lett.* **2018**, *18*, 3017.

[44] Y. Q. Fu, S. Zhang, M. J. Wu, W. M. Huang, H. J. Du, J. K. Luo, A. J. Flewitt, W. I. Milne, *Thin Solid Films* **2006**, *515*, 80.

[45] a) E. Lee, J. M. Lee, J. H. Koo, W. Lee, T. Lee, *Int. J. Hydrogen Energy* **2010**, *35*, 6984; b) L. G. Villanueva, F. Fargier, T. Kiefer, M. Ramonda, J. Brugger, F. Favier, *Nanoscale* **2012**, *4*, 1964.

[46] A. Ishida, M. Sato, *Acta Mater.* **2003**, *51*, 5571.

[47] J. D. Busch, A. D. Johnson, C. H. Lee, D. A. Stevenson, *J. Appl. Phys.* **1990**, *68*, 6224.

[48] P. Krulevitch, P. B. Ramsey, D. M. Makowiecki, A. P. Lee, M. A. Northrup, G. C. Johnson, *Thin Solid Films* **1996**, *274*, 101.

[49] M. Kohl, D. M. Allen, T. T. Chen, S. Miyazaki, M. Schwörer, *Mater. Sci. Eng. A* **1999**, *270*, 145.

[50] F. Gallucci, E. Fernandez, P. Corengia, M. van Sint Annaland, *Chem. Eng. Sci.* **2013**, *92*, 40.

[51] J. Tong, R. Shirai, Y. Kashima, Y. Matsumura, *J. Membr. Sci.* **2005**, *260*, 84.

[52] X. Gu, Z. Lu, H. Jiang, T. Akita, Q. Xu, *J. Am. Chem. Soc.* **2011**, *133*, 11822.

[53] E. Lee, J. M. Lee, J. H. Koo, W. Lee, T. Lee, *Int. J. Hydrogen Energy* **2010**, *35*, 6984.

[54] M. Vlček, F. Lukáč, M. Vlach, S. Wagner, C. Baehtz, A. Shalimov, A. Pundt, J. Čížek, *J. Alloys Compd.* **2015**, *645*, S446.

[55] S. Wagner, T. Kramer, H. Uchida, P. Dobron, J. Cizek, A. Pundt, *Acta Mater.* **2016**, *114*, 116.

[56] B. Xu, Z. Tian, J. Wang, H. Han, T. Lee, Y. Mei, *Sci. Adv.* **2018**, *4*, eaap8203.

[57] W. Huang, S. Koric, X. Yu, K. J. Hsia, X. Li, *Nano Lett.* **2014**, *14*, 6293.

[58] Y. Mei, S. Kiravittaya, S. Harazim, O. G. Schmidt, *Mater. Sci. Eng. R* **2010**, *70*, 209.

[59] Z. Chen, G. S. Huang, I. Trase, X. M. Han, Y. Mei, *Phys. Rev. A* **2016**, *5*, 17001.

[60] L. Zhang, E. Ruh, D. Gruetzmacher, L. Dong, D. J. Bell, B. J. Nelson, C. Schoenenberger, *Nano Lett.* **2006**, *6*, 1311.

[61] L. Zhang, E. Deckhardt, A. Weber, C. Schonenberger, D. Grutzmacher, *Nanotechnology* **2005**, *16*, 655.

[62] D. J. Bell, L. Dong, B. J. Nelson, M. Golling, L. Zhang, D. Grützmacher, *Nano Lett.* **2006**, *6*, 725.

[63] Z. Tian, W. Huang, B. Xu, X. Li, Y. Mei, *Nano Lett.* **2018**, *18*, 3688.

[64] P. Cendula, S. Kiravittaya, Y. F. Mei, C. Deneke, O. G. Schmidt, *Phys. Rev. B Condens. Matter* **2009**, *29*, 085429.

[65] X. Cheng, Y. Zhang, *Adv. Mater.* **2019**, *31*, 1901895.

[66] C. Py, P. Reverdy, L. Doppler, J. Bico, B. Roman, C. N. Baroud, *Phys. Rev. Lett.* **2007**, *98*, 156103.

**ADVANCED
SCIENCE NEWS**

www.advancedsciencenews.com

**ADVANCED
INTELLIGENT
SYSTEMS**
Open Access

www.advintellsyst.com

[67] J. Cho, A. Azam, D. H. Gracias, *Langmuir* **2010**, *26*, 16534.

[68] K. Kirshenbaum, D. C. Bock, C. Y. Lee, Z. Zhong, K. J. Takeuchi, A. C. Marschilok, E. S. Takeuchi, *Science* **2015**, *347*, 149.

[69] B. H. Kim, J. Lee, S. M. Won, Z. Xie, J. Chang, Y. Yu, Y. K. Cho, H. Jang, J. Y. Jeong, Y. Lee, A. Ryu, D. H. Kim, K. H. Lee, J. Y. Lee, F. Liu, X. Wang, Q. Huo, S. Min, D. Wu, B. Ji, A. Banks, J. Kim, N. Oh, H. M. Jin, S. Han, D. Kang, C. H. Lee, Y. M. Song, Y. Zhang, Y. Huang, et al., *ACS Nano* **2018**, *12*, 4164.

[70] L. Gao, Y. Zhang, H. Zhang, S. Doshay, X. Xie, H. Luo, D. Shah, Y. Shi, S. Xu, H. Fang, J. A. Fan, P. Nordlander, Y. Huang, J. A. Rogers, *ACS Nano* **2015**, *9*, 5968.

[71] H. Fu, K. Nan, W. Bai, W. Huang, K. Bai, L. Lu, C. Zhou, Y. Liu, F. Liu, J. Wang, M. Han, Z. Yan, H. Luan, Y. Zhang, Y. Zhang, J. Zhao, X. Cheng, M. Li, J. W. Lee, Y. Liu, D. Fang, X. Li, Y. Huang, Y. Zhang, J. A. Rogers, *Nat. Mater.* **2018**, *17*, 268.

[72] M. M. Qazilbash, M. Brehm, B. Chae, P. C. Ho, G. O. Andreev, B. Kim, S. J. Yun, A. V. Balatsky, M. B. Maple, F. Keilmann, H. Kim, D. N. Basov, *Science* **2007**, *318*, 1750.

[73] K. Wang, C. Cheng, E. Cardona, J. Guan, K. Liu, J. Wu, *ACS Nano* **2013**, *7*, 2266.

[74] K. Liu, C. Cheng, Z. Cheng, K. Wang, R. Ramesh, J. Wu, *Nano Lett.* **2012**, *12*, 6302.

[75] T. Wang, D. Torres, F. E. Fernandez, C. Wang, N. Sepulveda, *Sci. Adv.* **2017**, *3*, e1602697.

[76] K. Liu, C. Cheng, J. Suh, R. Tang-Kong, D. Fu, S. Lee, J. Zhou, L. O. Chua, J. Wu, *Adv. Mater.* **2014**, *26*, 1746.

[77] H. Ma, J. Hou, X. Wang, J. Zhang, Z. Yuan, L. Xiao, Y. Wei, S. Fan, K. Jiang, K. Liu, *Nano Lett.* **2017**, *17*, 421.

[78] Y. Fu, H. Du, W. Huang, S. Zhang, M. Hu, *Sens. Actuators A* **2004**, *112*, 395.

[79] J. J. Gill, D. T. Chang, L. A. Momoda, G. P. Carman, *Sens. Actuators A* **2001**, *2*, 148.

[80] Y. Q. Fu, J. K. Luo, A. J. Flewitt, S. E. Ong, S. Zhang, H. J. Du, W. I. Milne, *Int. J. Surf. Sci. Eng.* **2009**, *2*, 208.

[81] M. Mizumoto, T. Ohgai, A. Kagawa, *J. Alloys Compd.* **2009**, *482*, 416.

[82] A. Ollagnier, A. Fabre, T. Thundat, E. Finot, *Sens. Actuators B* **2013**, *186*, 258.

[83] H. Han, S. Baik, B. Xu, J. Seo, S. Lee, S. Shin, J. Lee, J. H. Koo, Y. Mei, C. Pang, T. Lee, *Adv. Funct. Mater.* **2017**, *27*, 1701618.

[84] N. Bassik, A. Brafman, A. M. Zarafshar, M. Jamal, D. Luvsanjav, F. M. Selaru, D. H. Gracias, *J. Am. Chem. Soc.* **2010**, *132*, 16314.

[85] X. Chen, L. Mahadevan, A. Drikes, O. Sahin, *Nat. Nanotechnol.* **2014**, *9*, 137.

[86] M. Medina-Sánchez, V. Magdanz, M. Guix, V. M. Fomin, O. G. Schmidt, *Adv. Funct. Mater.* **2018**, *28*, 1707228.

[87] Y. Kim, H. Yuk, R. Zhao, S. A. Chester, X. Zhao, *Nature* **2018**, *558*, 274.

[88] E. Merced, X. Tan, N. Sepúlveda, *Sens. Actuators A* **2013**, *196*, 30.

[89] P. Krulevitch, A. P. Lee, P. B. Ramsey, J. C. Trevino, J. Hamilton, M. A. Northrup, *J. Microelectromech. Syst.* **1996**, *5*, 270.

[90] S. Wagner, T. Kramer, H. Uchida, P. Dobron, J. Cizek, A. Pundt, *Acta Mater.* **2016**, *114*, 116e125.